Electronic Supplementary Material (ESI) for Physical Chemistry Chemical Physics.

Supporting Information

Tin doping speeds up light-driven water oxidation at hematite photoanodes

Halina K. Dunn,[1§] Johann M. Feckl,[1§] Alexander Müller,[1] Dina Fattakhova-Rohlfing,[1] Samuel G. Morehead,[1] Julian Roos,[1] Laurence M. Peter,[2] Christina Scheu,[1] Thomas Bein[1,]**

[1]Department of Chemistry and Center for Nanoscience (CeNS), Ludwig-Maximilians-Universität München, Butenandtstr. 11, D-81377 Munich, Germany

[2]Department of Chemistry, University of Bath, BA2 7AY, Bath, United Kingdom

[§] These authors contributed equally

Received Date:

e-mail: bein@lmu.de, halina.dunn@cup.lmu.de

Further synthetic details

Table 1: Molar ratio of Sn to Fe precursors for the different doping concentrations, all other synthetic details can be found in the experimental section of the main text.

	$Fe(NO_3)_3 \cdot 9\ H_2O$		$Sn(OAc)_4$	
Sn:Fe ratio [%]	[g]	[mmol]	[g]	[mmol]
0	0.630	1.56	-	-
5	0.598	1.48	0.025	0.070
10	0.568	1.41	0.055	0.156
15	0.537	1.33	0.083	0.234
20	0.505	1.25	0.111	0.313
30	0.440	1.09	0.166	0.470

Powder XRD

The powder XRD patterns in Figure SI 1 exclusively show the α-Fe_2O_3 hematite phase, with a peak shift of approximately 0.1° to smaller angles upon Sn-doping (20 % sample), indicating a lattice distortion brought about by inclusion of impurity atoms.[1] This shift corresponds to an increase of the lattice parameter, *a*, from 5.036 to 5.043 Å, which is not visible in HRTEM images due to insufficient image resolution, see Figure 8. Additionally, the inversion of intensities of the two reflections in the range of 33 to 36° 2θ is observed, similar to a Sn-doped hematite described by Berry *et al.*[1] The mean crystallite size, as calculated from the broadening of the (104) reflection according to the Scherrer equation, drops from 50 to 30 nm upon inclusion of Sn. This is in agreement with the slight reduction in particle size upon Sn-inclusion observed

in SEM. Hence, our XRD, SEM and TEM investigations agree on a reduction in feature size upon Sn-incorporation. Although this observation fits the general trend, we note that this change in feature size is less extreme than in other reports, such as the reduction in hematite nanowire length from 600 to 100 nm upon Sn-doping reported by Ling *et al.*[2]

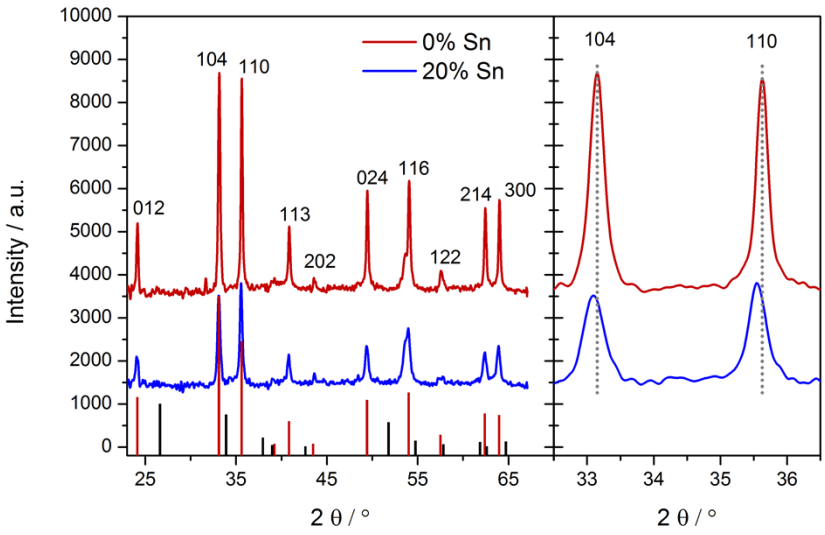

Figure SI 1: Powder XRD data of hematite layers prepared with 0 % and 20 % Sn-precursor in the synthesis. Below the ICDD card 01-085-0987 of hematite (red) and the ICDD card 01-075-9493 of SnO_2 (black). The right hand panel shows the peak shift attributed to lattice distortion upon inclusion of Sn-atoms.

Further details on morphology and estimation of the surface roughness factor

Figure 3 of the main text illustrates the effect of Sn doping on the morphology of the films. The morphology remains unchanged up to the addition of 20 % Sn-precursor to the synthesis. However, we note the appearance of larger bright features in the 10 % Sn-doped samples, and to a larger extent 20 % Sn-doped samples. The large crystals of the FTO substrate (see SEM cross section of 20 %-doped sample, Figure 3) protrude into the overlying film of hematite. These

features are usually covered with structured Sn-doped hematite which can be seen most clearly in the SEM top view oft he 20 % Sn-doped film. The increasing appearance of these bright features (and therefore the lower coverage by the overlying hematite layer) can be explained by an artefact related to the film preparation. These were prepared with a given amount of metal precursor in the spin coating solution, and so the higher the concentration of Sn-precursor, the lower the concentration of Fe-precursor, which leads to slightly thinner Sn-doped layers." These findings are also supported by Absorbance measurements, see Figure SI 4c, which show a lower absorbance of the Sn-doped films compared to the undoped films.

The surface area of the 0 % and 20 % Sn films was estimated by approximating their structure by a monolayer of close-packed half cylinders with rounded ends, as depicted in Figure SI 2. Average values of the length, *L*, and width, *W*, of the particles were determined by inspecting 10 random nanoparticles in the SEM images seen in Figure 3. The geometric enhancement factor is defined as $S/(W \times L)$, where the surface area, *S*, is defined by equation* MERGEFORMAT (SI 1). In this way, geometric enhancement factors of 2.5 and 2.4 were estimated for the 20 % and 0 % Sn-samples, respectively.

$$S = \frac{1}{2}\pi\left[W\left(L-W\right)+W^2\right] \qquad \text{* MERGEFORMAT (SI 1)}$$

The total volume of such cylinders, as well as the volume of the bulk of the cylinders (excluding the space charge region), are respectively:

$$V_{total} = \frac{1}{2}\left[\pi\left(\frac{W}{2}\right)^2\left(L-W\right)+\frac{4}{3}\pi\left(\frac{W}{2}\right)^3\right] \qquad \text{* MERGEFORMAT (SI 2)}$$

$$V_{bulk} = \frac{1}{2}\left[\pi\left(\frac{W}{2} - W_{SC}\right)^2 (L - W) + \frac{4}{3}\pi\left(\frac{W}{2} - W_{SC}\right)^3\right] \backslash^* \text{ MERGEFORMAT}$$

(SI 3)

The geometrical enhancement factor was needed for the Mott-Schottky analysis, and the volumes for the estimate of η_{sep}, see below.

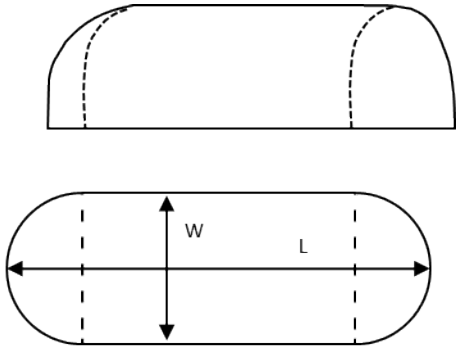

Figure SI 2: Geometrical approximation used to estimate the geometrical enhancement of the photoanode surface area.

Electron diffraction data

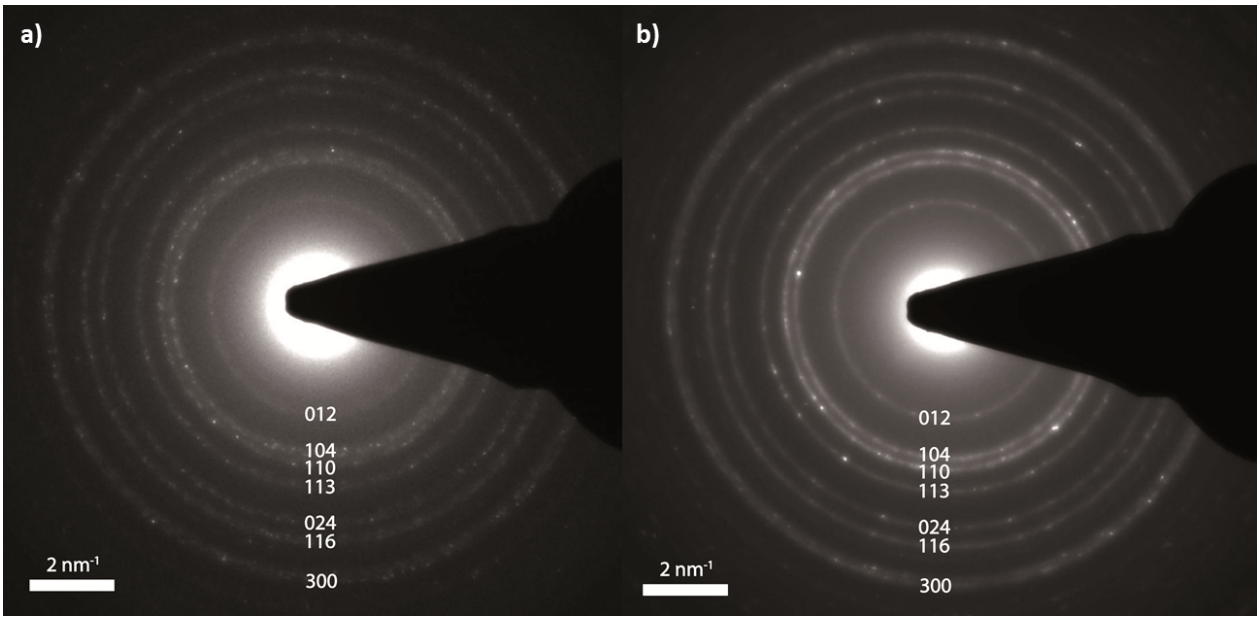

Figure SI 3: Electron diffraction patterns obtained in TEM of a) 20 % and b) 0 % Sn samples.

Diffraction patterns of several hundred particles confirmed the hematite structure, to which all reflections could be assigned.

Light harvesting

In order to quantify the light harvesting efficiency of the photo-anodes, multilayer-films with thicknesses ranging from approximately 50 to 400 nm were prepared. Inspection of SEM cross-sectional images (such as those of 1 and 3 layer films, which can be seen in Figure SI 4a and b) suggest that the film thickness scales well with the number of layers, with each layer contributing around 50 nm. This is confirmed by the UV-visible absorption spectra, calculated according to equation (9) in the main text, which are shown in Figure SI 4c. The absorbance at 400 nm is shown in Figure SI 4d as a function of thickness for pure hematite films, as well as 20 % Sn films. A linear regression of the absorbance as a function of thickness yielded an apparent absorption coefficient, $\alpha(400\,\text{nm})$, of $1.59 \times 10^5\,\text{cm}^{-1}$ for the pure hematite sample, and $1.35 \times 10^5\,\text{cm}^{-1}$ for the sample prepared with 20 % Sn in the precursor. These values can be

compared with α(400nm) = 2.2 x 10^5 cm^{-1} reported by Klahr *et al.*[3] for compact layers of hematite prepared by ALD. The lower observed absorption coefficients of our material are attributed to its porous nature.

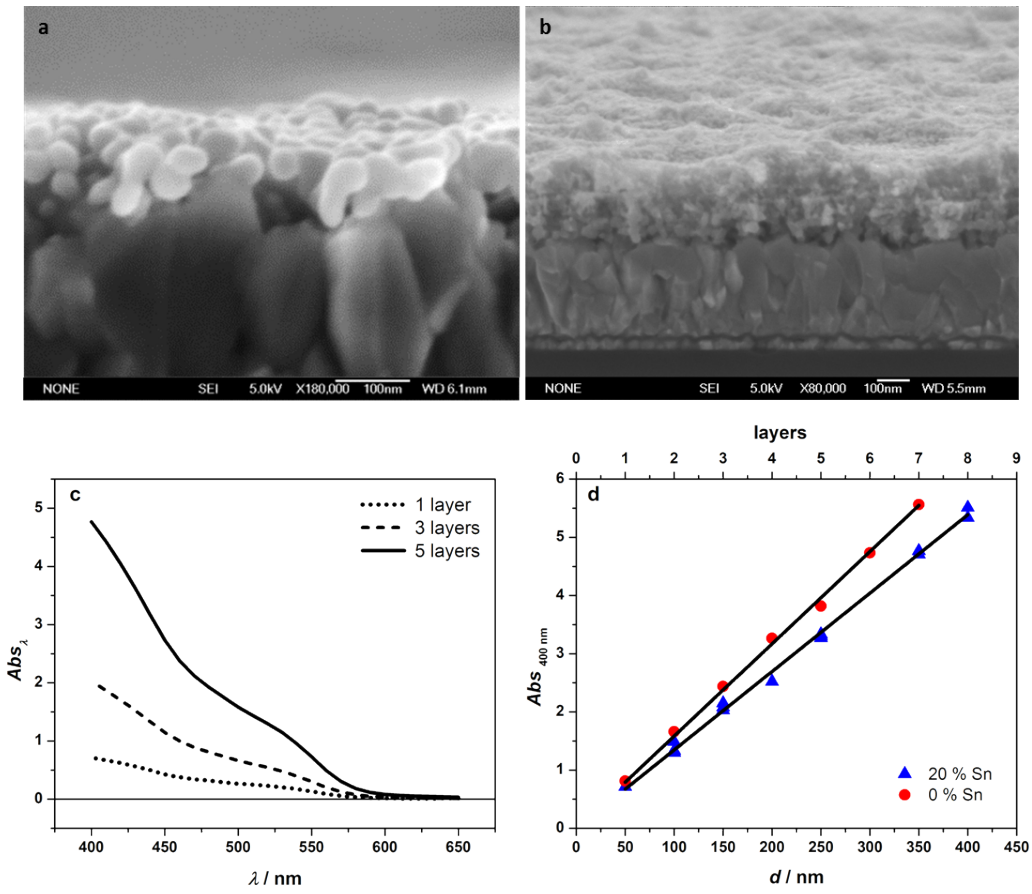

Figure SI 4: Thickness, morphology and optical properties of multilayer films. Unless otherwise stated, all films were prepared with 20 % Sn-precursor added to the synthesis. SEM cross sections of 1 (a, undoped) and b) 3 layered films. c) UV-visible absorption spectra of 1, 3and 7 layer films. d) Absorbance at 400 nm as a function of the number of layers (blue triangles). For comparison, the absorbance at 400 nm of multi-layer films of pure hematite is included (red circles).

Dark cyclic voltammetry

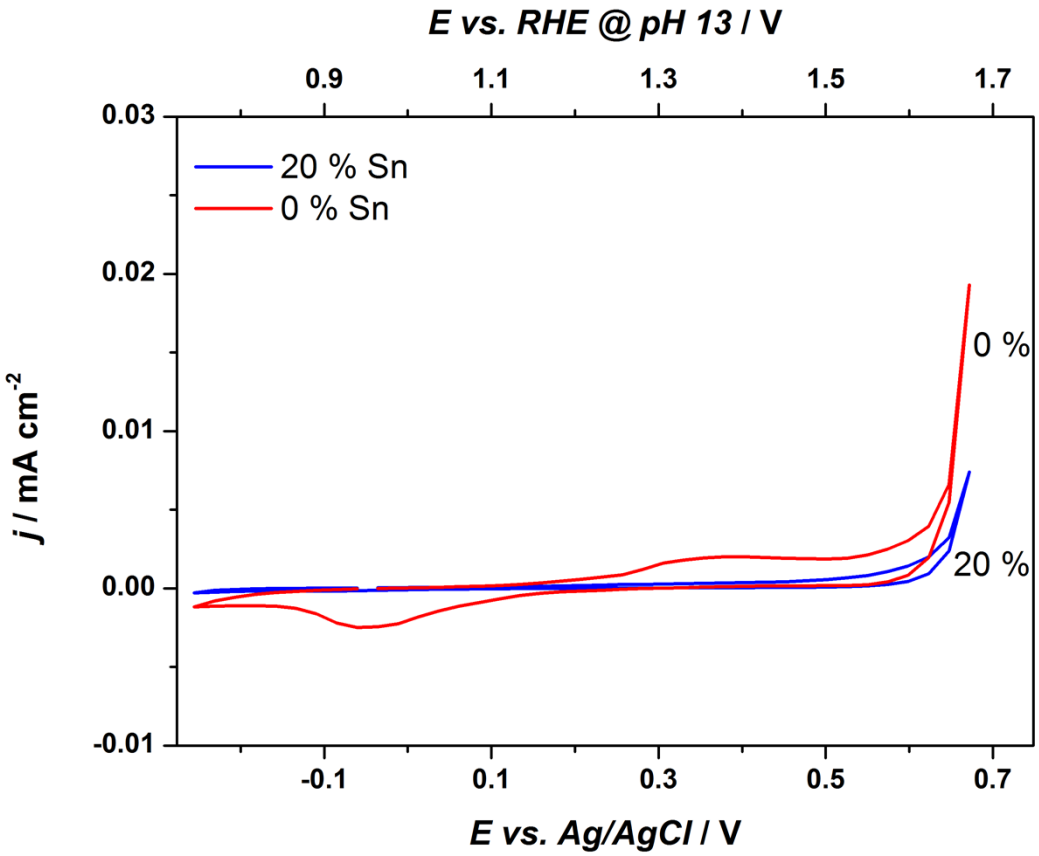

Figure SI 5: Dark cyclic voltammograms of pure hematite and of hematite prepared with 20 % Sn-precursor in the synthesis.

Evaluation of the 20 % Sn thin films as model systems

In this work, we studied the role of Sn-inclusion in enhancing the PEC performance of hematite. The thin films used in the study satisfy the following criteria: well-defined absorbance, limited morphological change upon Sn inclusion and a space charge layer thickness smaller than the feature size (see below). Due to their modest light-harvesting efficiencies, the films produce lower photocurrents than the state of the art hematite photoanodes reported in the literature, see Figure SI 6.

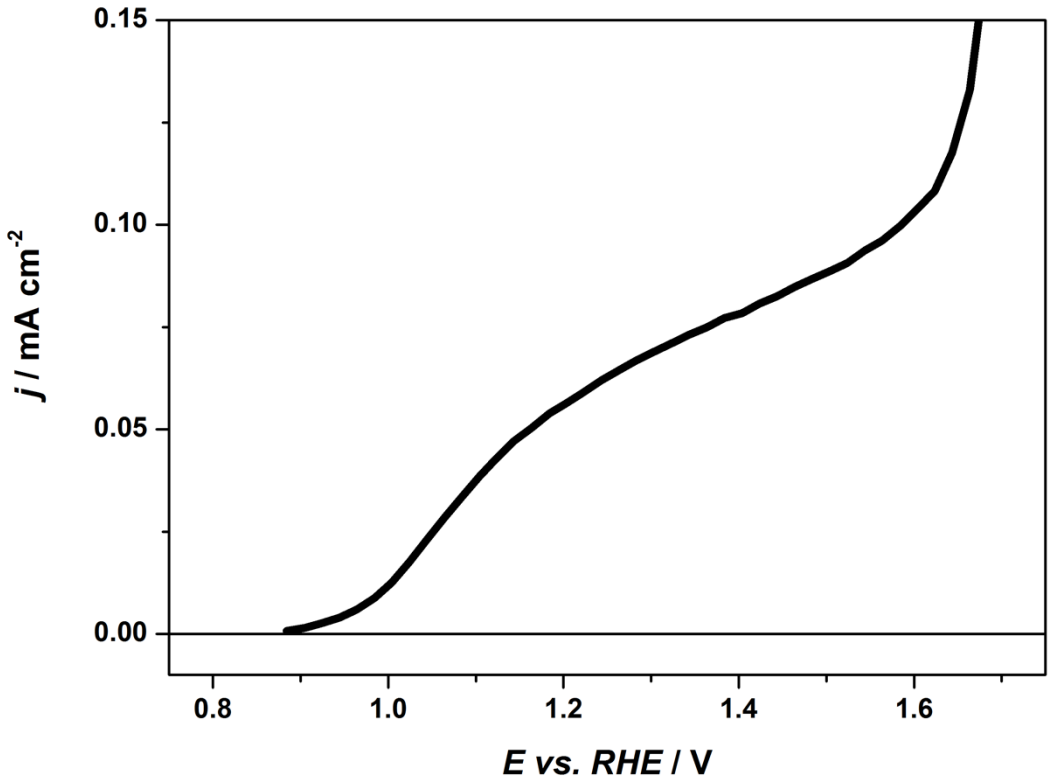

Figure SI 6: Steady state current density as a function of applied potential of a 50 nm thick 20 % Sn-doped sample under AM 1.5 illumination.

The EQE measured under AM 1.5 bias light close to the thermodynamic water oxidation potential, is shown in Figure SI 7a. During light-driven water oxidation, the EQE depends on the efficiencies of light harvesting, charge separation and hole-transfer to the electrolyte, according to equation (1) (main paper). The light harvesting efficiency, η_{LH} calculated from the absorbance according to equation (2) (main paper) is shown in Figure SI 7b, along with the transfer efficiency $\eta_{trans} = k_{trans}/(k_{trans} + k_{rec})$ determined under similar conditions from IMPS analysis. Since the EQE is known, knowledge of η_{trans} and η_{LH} gives access to the separation efficiency, η_{sep}, which is also shown in Figure SI 7b. Under standard operating conditions, the separation

efficiency is clearly the main efficiency limiting process, with fewer than 10 % of absorbed photons resulting in a hole reaching the surface of the hematite. This result is in agreement with Dotan *et al*., [4] who found separation efficiencies between 10 and 15 % for high-performance Si-doped hematite prepared by atmospheric pressure chemical vapour deposition and ultrasonic spray pyrolysis under similar conditions. These authors also reported transfer efficiencies of the order of 25 %, in close agreement with our results. We thus conclude that although our films underperform relative to state of the art hematite electrodes, this is purely due to the modest light harvesting efficiency, and these films make good model systems for this study. The *j-V* characteristics of a 400 nm thick films of our material are shown in Figure SI 7. The thicker films give 0.38 mA cm^{-2} at 1.23 V vs. RHE under AM 1.5 illumination, which is very close to the photocurrent of benchmark solution-processed hematite photoanodes (0.38 mA cm^{-2} under the same conditions).[22] Nonetheless, thin films were used in the mechanistic studies since these constitute the simplest model system.

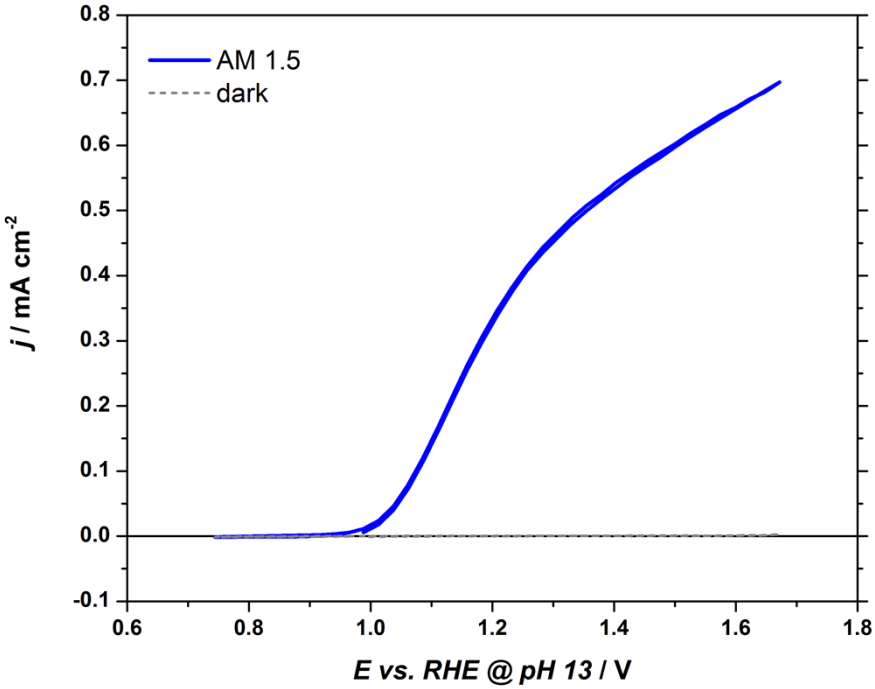

Figure SI 7: Steady state current density as a function of applied potential of a 400 nm thick 20 % Sn-doped sample under AM 1.5 illumination.

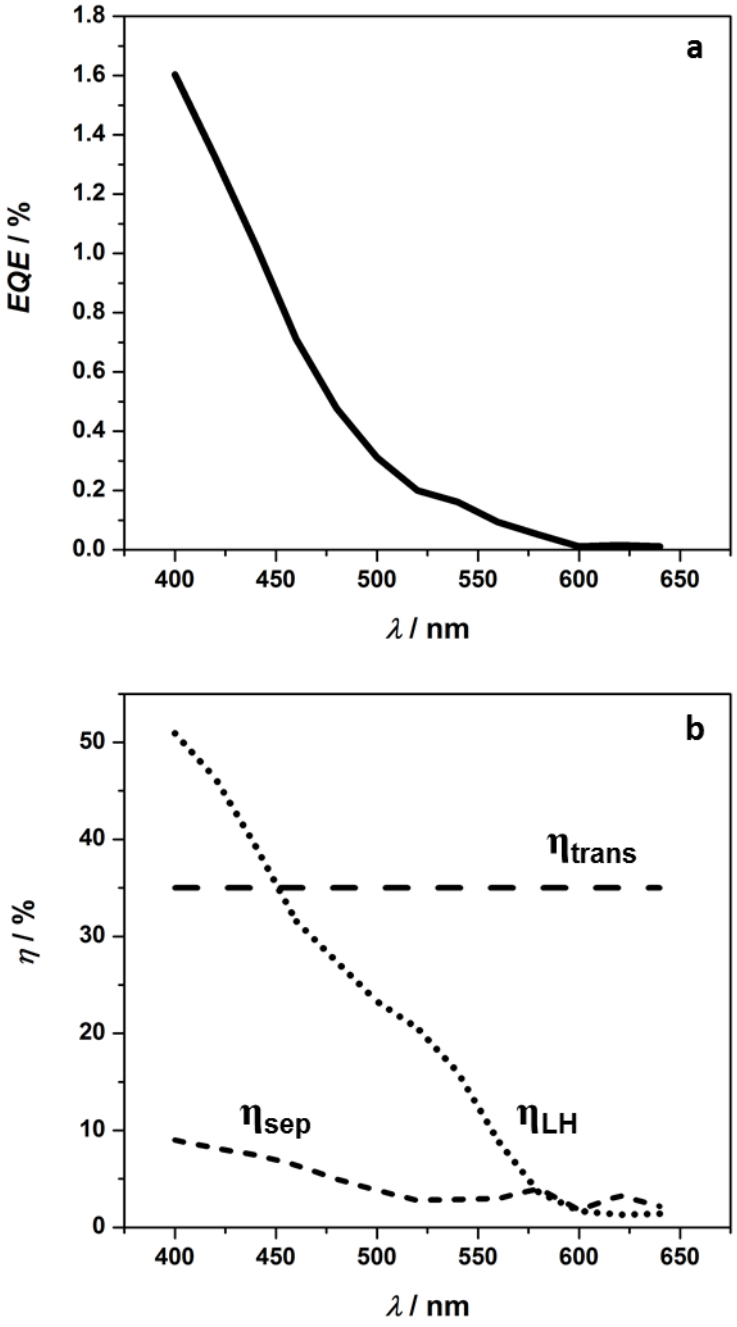

Figure SI 8: a) EQE of a 20 % Sn-doped sample measured under AM 1.5 background illumination close to the thermodynamic potential for water oxidation (1.194 V vs RHE). b) Efficiencies of light harvesting, charge separation and hole-transfer determined under identical conditions, where applicable.

Determination of the width of the space charge layer from Mott Schottky and Gärtner analysis

EIS data were fitted to the Randles' equivalent circuit shown in the inset of Figure SI 8, with parallel resistances, R_p, of the order of 10 kΩ cm^{-2} corresponding to the small dark current. The capacitances determined in this way are shown as Mott-Schottky plots in Figure SI 8. As these electrodes are not perfectly compact and uniform layers, the data are not linear over the entire range. However, at low applied anodic biases, a linear fit can be made, yielding flatband potentials, V_{fb}, of *ca.* 0.7 and 0.4 V vs RHE for 0 % and 20 % samples, respectively. Furthermore, the doping density, N_d, can be extracted from the slope of such plots, according to the Mott Schottky equation[5] (equation (5) in the main text). Assuming a relative permittivity of 25[6], and correcting the geometrical surface area with the roughness factor described above yields very similar doping densities of $3x10^{19}$ cm^{-3} and $1.5x10^{19}$ cm^{-3}, for the undoped and 20 % Sn-doped samples, respectively. We conclude from this that the Sn dopant is not acting as an electrical dopant in this case, and we can therefore rule out that the increase in photocurrent upon doping is due to an increase in conductivity. This is in good agreement with a recent study on Ti doped hematite by Zandi *et al.*.[7]

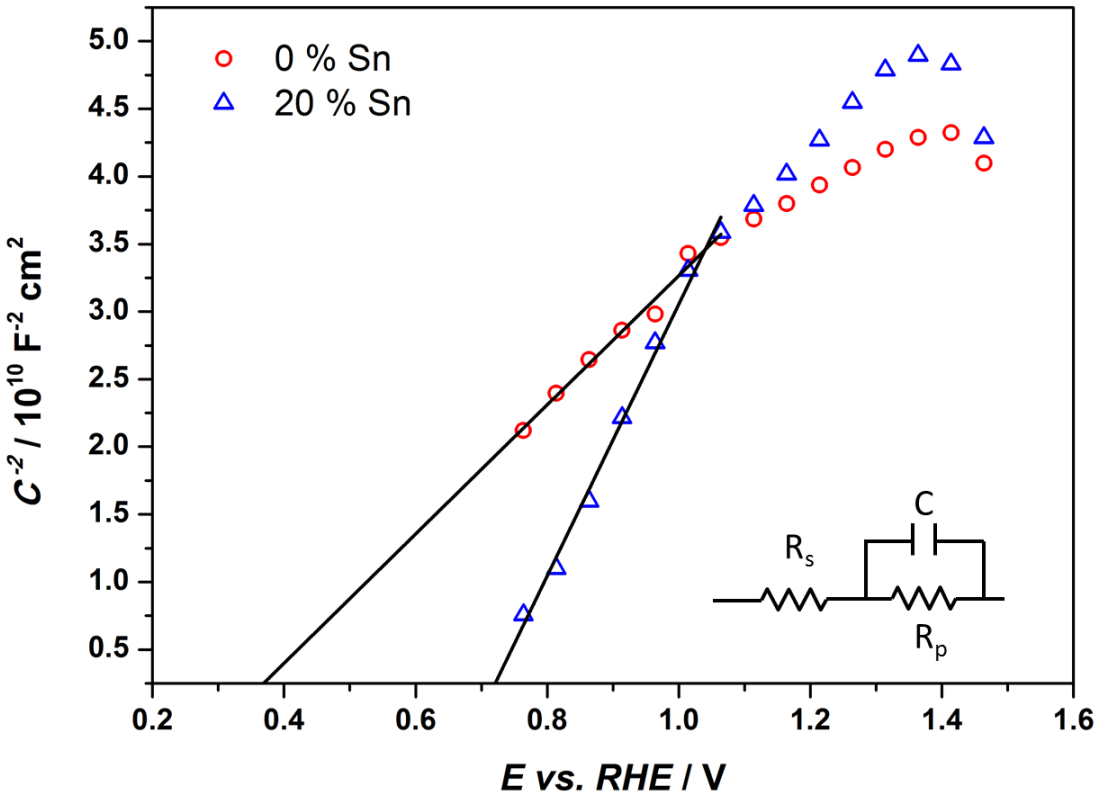

Figure SI 9: Mott-Schottky plots obtained from hematite photoanodes prepared with 0 % and 20 % Sn-precursor in the synthesis.

Another indicator of V_{fb} is the onset potential of anodic transient photoactivity.[8] The photocurrent-voltage curves under chopped illumination, shown in Figure SI 9, reveal that V_{fb} is of the order of 0.6 and 0.3 V vs RHE for the 0 % and 20 % photoanodes, respectively, in good agreement with the values determined from the Mott-Schottky analysis.

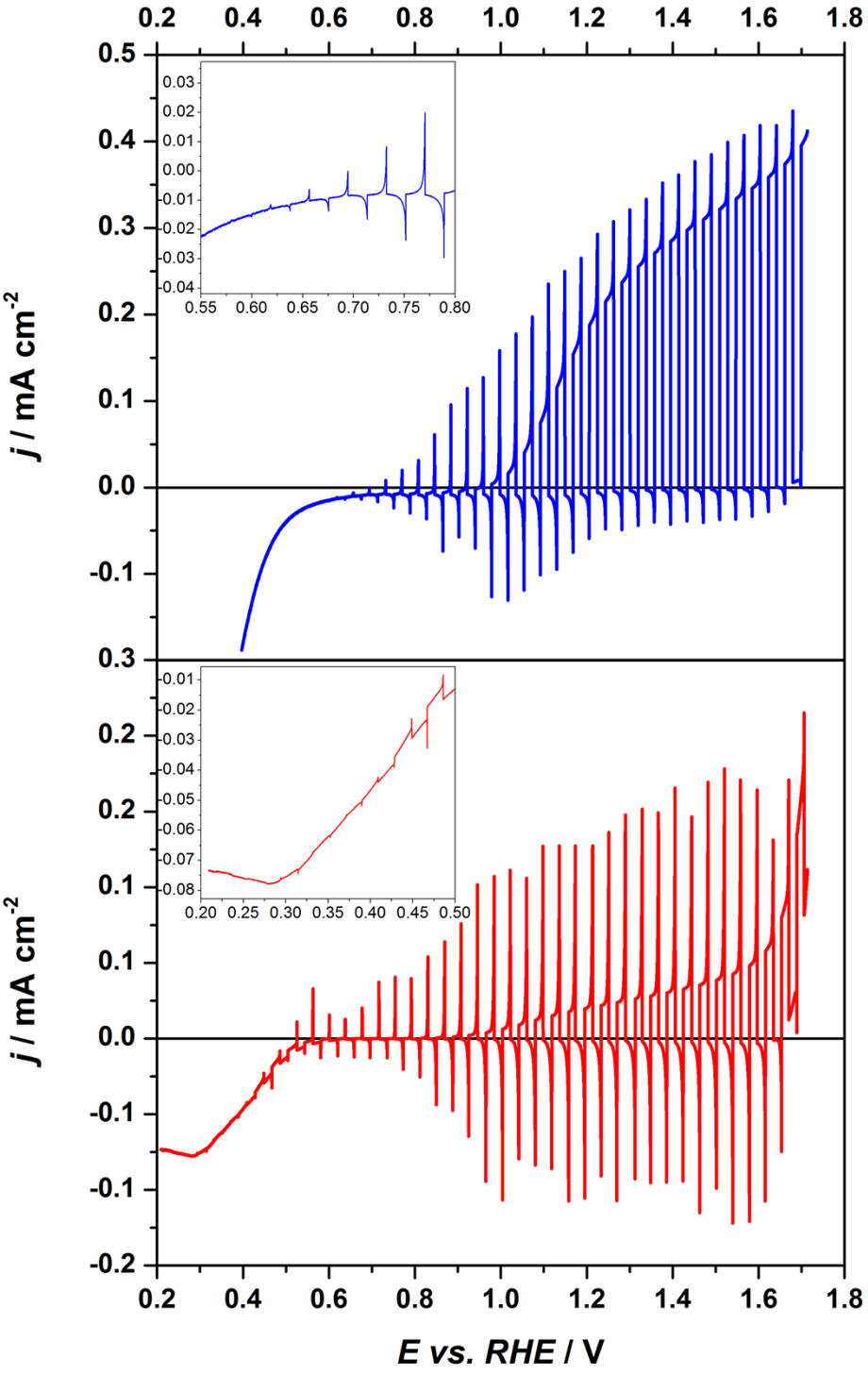

Figure SI 10: Current density under chopped illumination of hematite photoanodes prepared with 20 % (a) and 0 % (b) Sn-precursor in the synthesis. Monochromatic light (455 nm) chopped at 1 Hz, intensity ca. 10^{17} $cm^{-2}s^{-1}$, scan rate: 40 mVs^{-1}. The insets show the onset of transient photocurrent activity close to the flat band potential.

In order to calculate the doping density from the slopes of the Mott-Schottky plots according to equation (5) and the width of the space charge layer according to equation (6) (both equations are in the main text) the value of the dielectric constant, ε_r, is required. There is a wide range of ε_r values reported in the literature.[9,10] We have calculated W_{SC} from equation 6 with ε_r equal to 25[6] and 57[10] to illustrate the sensitivity of W_{SC} to this parameter, see Figure SI 10. For the higher value of the dielectric constant, the plots show that the assumption that the width of the space charge regions should be smaller than the particle radius, R will no longer be met for 30 nm particles, and the capacitance should saturate at high applied bias. However no experimental evidence for saturation of the capacitance was seen in the Mott-Schottky plots, and we therefore believe that the dielectric constant is small enough that the condition $W_{sc} < R$ is satisfied. This conclusion is supported by recent theoretical calculations that predict ε_r values close to 25.[6]

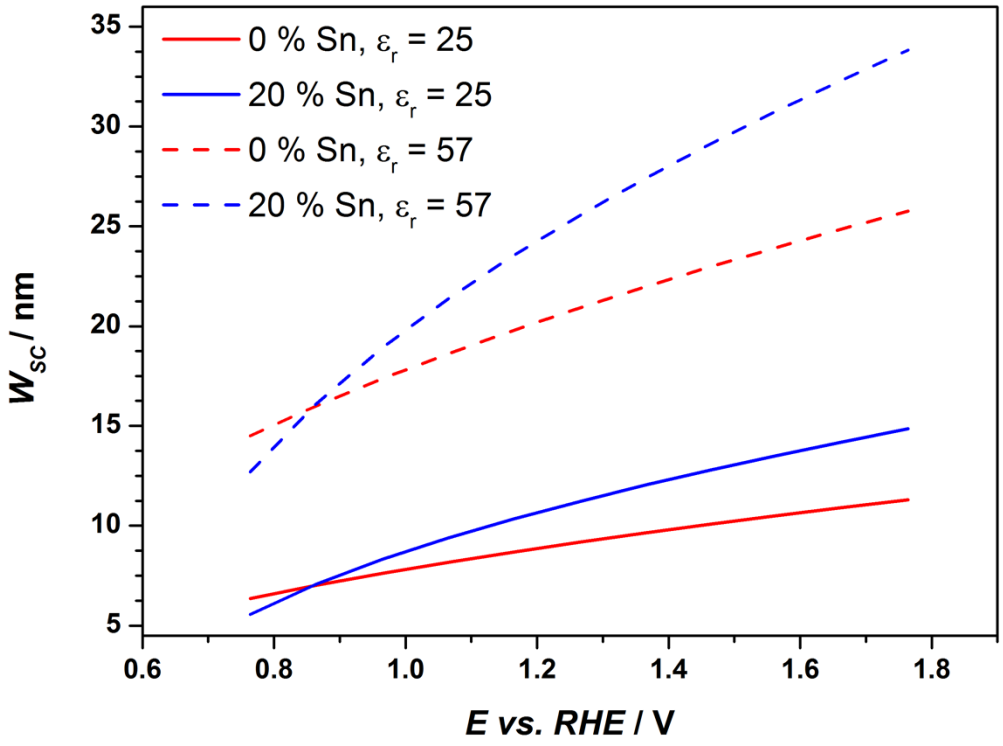

Figure SI 11: Calculated width of the space charge region for hematite photoanodes prepared with 0 % and 20 % Sn-precursor in the synthesis. V_{FB} was estimated from Mott-Schottky analysis and the transient anodic onset of photocurrent. For the pure hematite sample, donor densities of 3.2 x 10^{19}cm^{-3}, and of 1.3 x 10^{19}cm^{-3} were used in combination with dielectric constants of 25 and 57, respectively. For the Sn-enriched hematite sample, donor densities of 1.5 × 10^{19}cm^{-3}, and of 6.6 × 10^{18}cm^{-3} were used in combination with dielectric constants of 25 and 57, respectively.

Another method to estimate the width of the space charge layer is by use of the Gärtner equation (equations (7) and (8) in the main text).[11] In the present case, we have assumed that the product of the absorption coefficient α and the hole diffusion length L_p is much less than unity. The derivation of the Gärtner equation assumes that W_{sc} and L_p are considerably smaller than the thickness of the electrode. In addition, it is assumed that all holes reaching the surface are consumed in a rapid electron transfer reaction. In the case where some fraction of the hole flux is lost by recombination, a correction must be made using the transfer efficiency determined by IMPS, so that the EQE term in equation 8 should be replaced by EQE(k_{trans} + k_{rec})/k_{trans}, giving

equation 9. Using the values of α(400 nm), and the EQE and transfer efficiency data (which can be seen in Figure 5 and 7 of the main text) gives a value of W_{SC} of the order of 3 nm at a potential of 1.2 V vs. RHE under AM 1.5. This value is significantly lower than the one inferred from the Mott-Schottky analysis. As noted above, reported values for the dielectric constant of hematite range from 25 to 57, therefore assuming a lower value of ε_r in the calculation of W_{SC} from the Mott-Schottky analysis would bring it into better agreement with the Gärtner analysis. Alternatively, the width of the space charge layer could be different in the dark, as determined by Mott-Schottky plots, and under illumination, as determined by the Gärtner analysis. This would be the case if potential were dropped across a build-up of surface charges, rather than exclusively across the space charge region. Several studies have observed Fermi level pinning,[12,13] and it has been established spectroscopically that the slow OER kinetics lead to a significant build-up of surface holes.[14,15]

A weakness of the above Gärtner analysis is that it assumes that the electrode is flat, whereas in the present case it is nanostructured. A rough estimate of the separation efficiency (in the absence of recombination in the space charge region) can be obtained from the ratio of the space charge region volume to the total semiconductor volume, $\left(V_{tot} - V_{bulk}\right)/V_{tot}$ (*cf.* equations * MERGEFORMAT (SI 2) and * MERGEFORMAT (SI 3)), based on the geometry depicted in Figure SI 2. The result of this calculation is shown in Figure SI 11, which shows the separation efficiency as a function of the space charge layer width. As expected, the separation efficiency increases as the semiconductor becomes more depleted. From this calculation, a separation efficiency of around 0.1 (the value calculated at 400 nm from experimental data in Figure SI 7) is achieved with a depletion width of the order of a nanometer, providing further evidence that W_{SC}

is just a few nanometres under illumination. For such thin space charge layers, electron-hole recombination by tunnelling becomes possible, and this as well as space charge layer recombination may explain the low values of W_{sc} obtained from the analysis of the EQE.

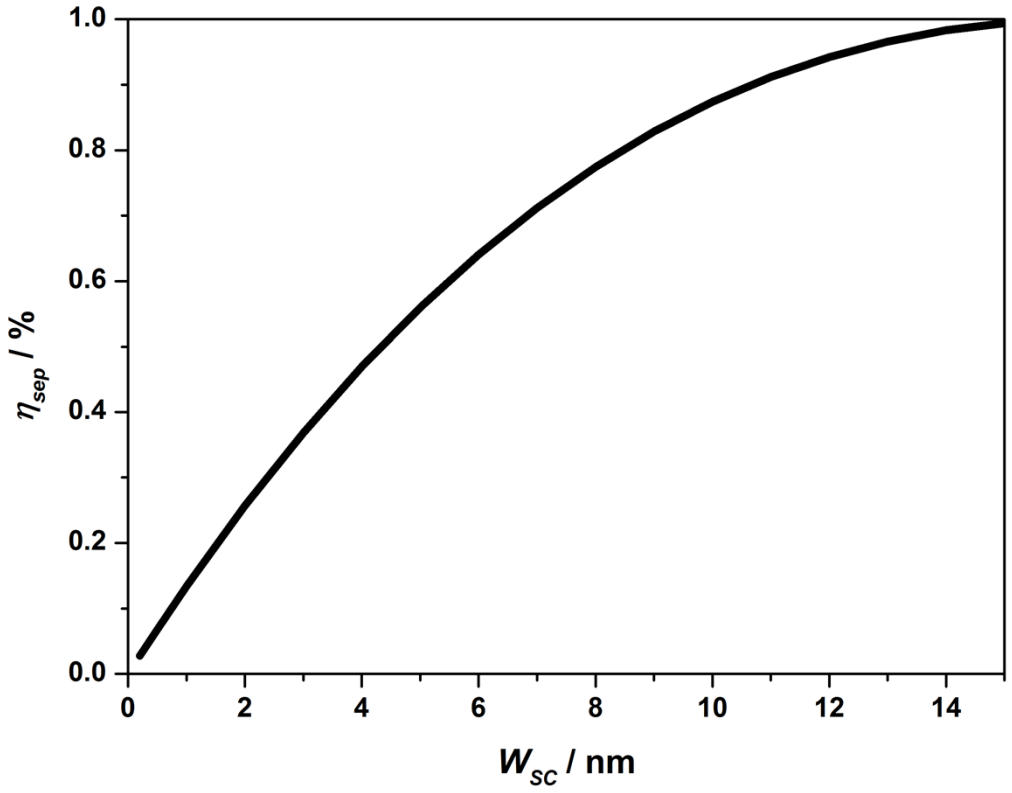

Figure SI 12: Separation efficiency estimated geometrically as a function of the space charge width.

We therefore conclude that under illumination, W_{SC} is of the order of a few nanometres, and is thus significantly smaller than the particle size, implying that the particles are not fully depleted. This makes the analysis of transients and IMPS according to the model for compact electrodes described in the main paper possible. We note that to be fully reliable, experiments should be

carried out as small amplitude perturbations (such as IMPS and the EQE measured under bias light presented here) in order to assure the band bending is not changing during the experiment.

Further data derived from IMPS

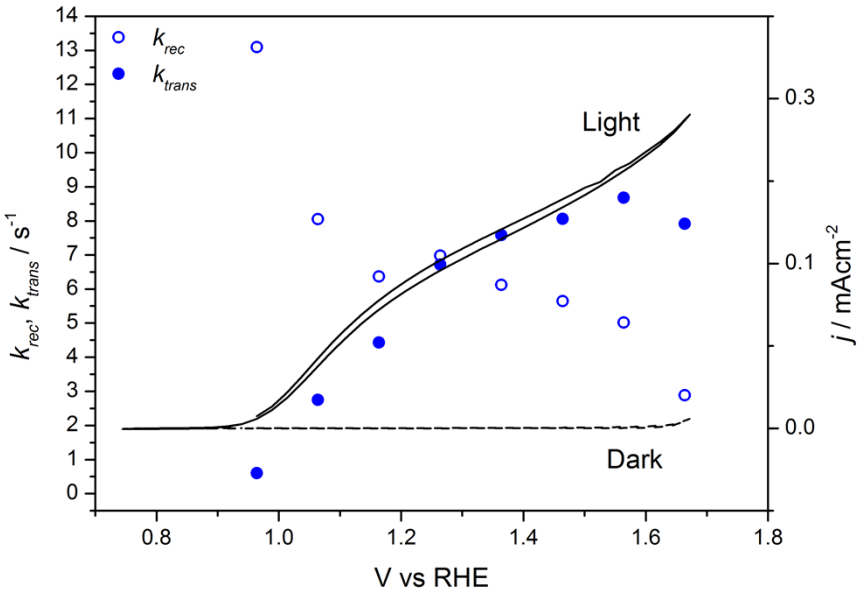

Figure SI 13: Transfer- (filled circles) and recombination- (empty circles) rate constants obtained from IMPS overlaid with the J-V characteristics in the dark (broken line) and under illumination (full line) for the 20 % sample. Illumination was provided by a 470 nm LED, intensity 10^{17} cm^{-2}s^{-1} in all cases.

The rates of recombination and transfer for the 20 % Sn doped sample are shown in Figure SI 12. Equation 3 in the main text shows that the transfer efficiency should be 0.5 when the rates of recombination and transfer are equal. The transfer efficiency reaches 0.5 at approximately 1.2 V *vs.* RHE (see Figur 7a), which coincides with the crossover between k_{trans} and k_{rec}, plots shown in Figure SI 12 b. Also shown in Figure SI 12 b are the *J-V* characteristics of the film. From this it can be seen that the crossover between k_{trans} and k_{rec} occurs at a potential at which the photoanode reaches approximately half of its maximum photocurrent. This good agreement between the

kinetic parameters obtained from IMPS and the steady state photocurrent data demonstrates the utility of the IMPS method in this case.

References

(1) Berry, F. J.; Greaves, C.; McManus, J. G.; Mortimer, M.; Oates, G. *Journal of Solid State Chemistry* **1997**, *130*, 272.

(2) Ling, Y.; Wang, G.; Wheeler, D. A.; Zhang, J. Z.; Li, Y. *Nano Lett.* **2011**, *11*, 2119.

(3) Klahr, B. M.; Martinson, A. B. F.; Hamann, T. W. *Langmuir* **2011**, *27*, 461.

(4) Dotan, H.; Sivula, K.; Gratzel, M.; Rothschild, A.; Warren, S. C. *Energy Environ. Sci.* **2011**, *4*, 958.

(5) Morrison, S. R. *Electrochemistry at Semiconductor and Oxidized Metal Electrodes*; Plenium Press, 1980.

(6) Lunt, R. A.; Jackson, A. J.; Walsh, A. *Chemical Physics Letters* **2013**, *586*, 67.

(7) Zandi, O., Klahr, B.M., Hamann, T.W. *Energy & Environmental Science* **2013**, *6*.

(8) Dareedwards, M. P.; Goodenough, J. B.; Hamnett, A.; Trevellick, P. R. *Journal of the Chemical Society-Faraday Transactions I* **1983**, *79*, 2027.

(9) Lunt, R.; Jackson, A.; Walsh, A. *Chem. Phys. Lett.* **2013**, *586*, 67.

(10) Glasscock, J. A.; Barnes, P. R. F.; Plumb, I. C.; Bendavid, A.; Martin, P. J. *Thin Solid Films* **2008**, *516*, 1716.

(11) Gärtner, W. W. *Physical Review* **1959**, *116*.

(12) Wijayantha, K. G. U.; Saremi-Yarahmadi, S.; Peter, L. M. *Phys. Chem. Chem. Phys.* **2011**, *13*, 5264.

(13) Klahr, B.; Gimenez, S.; Fabregat-Santiago, F.; Hamann, T.; Bisquert, J. *Journal of the American Chemical Society* **2012**, *134*, 4294.

(14) Cummings, C. Y.; Marken, F.; Peter, L. M.; Wijayantha, K. G. U.; Tahir, A. A. *Journal of the American Chemical Society* **2012**, *134*, 1228.

(15) Pendlebury, S. R.; Cowan, A. J.; Barroso, M.; Sivula, K.; Ye, J.; Graetzel, M.; Klug, D. R.; Tang, J.; Durrant, J. R. *Energy & Environmental Science* **2012**, *5*, 6304.